

# Investigating Ground Deformation and Possible Causative Factors in Menengai, Nakuru

Joline Achieng, Mercy Mwaniki

Department of Geomatic Engineering and Geospatial Information Systems, Jomo Kenyatta University of Agriculture and Technology, Nairobi, Kenya  
Email: jolieachieng@gmail.com

**How to cite this paper:** Achieng, J. and Mwaniki, M. (2023) Investigating Ground Deformation and Possible Causative Factors in Menengai, Nakuru. *International Journal of Geosciences*, 14, 1100-1122.  
<https://doi.org/10.4236/ijg.2023.1411056>

**Received:** October 11, 2023

**Accepted:** November 21, 2023

**Published:** November 24, 2023

Copyright © 2023 by author(s) and Scientific Research Publishing Inc.  
This work is licensed under the Creative Commons Attribution International License (CC BY 4.0).

<http://creativecommons.org/licenses/by/4.0/>



Open Access

## Abstract

Ground deformation measurements are important indicators of subsurface changes which may inform potentially catastrophic events such as structural damage to buildings or dams, derauling of rail lines, and slope failure. Consequently, there is a need for studies to quantify these measurements especially in areas predisposed due to these conditions. One such area is the Menengai caldera in the East African rift where faulting, magmatism and large-scale human activities are happening. This research investigates the magnitude of deformation experienced in Menengai-Subukia area and the relationship with spatial distribution of active faults and human activities such as geothermal development and land use. Sentinel 1 images for the duration 2015 to 2021 were processed in the Sentinel Application Platform (SNAP) using the Terrain Observation with Progressive Scans SAR (TOPSAR) technique. The interferograms showed that subsidence exists within Menengai Geothermal Field (MGF). Structural mapping consisted of automatic lineament extraction in PCI Geomatica using Sentinel 1 images to generate line density map accompanied with Rose diagram which showed concentration and orientation of faults. These faults are attributed to the uplift and subsidence in Menengai caldera due to extension of the stress regime of magma activity below the caldera. Supervised image classification was carried out on Sentinel 2 images in ENVI to generate Land Use Land Cover maps. Validation was done for some reference points (geothermal wells/power plants) and compared with results from the interferograms. This was done by fitting a graphical model of the GPS data and corresponding deformation obtained from the Sentinel 1 interferograms. The findings suggest that the most probable cause of deformation in the area is due to geothermal activities and groundwater abstraction. These techniques, coupled with continuous monitoring could be useful for land-use planning and prediction of geological hazards.

---

## Keywords

Deformation, InSAR, Menengai, Geothermal, Faulting

---

## 1. Introduction

Ground deformation is a manifestation of interplay between surface and sub-surface Earth processes largely controlled by active geological structures and underlying rock formations. Natural processes such as volcanic activity (magmatism) and faulting accentuate the deformation processes especially in rift environments [1]. Geothermal activity such as magmatism, fluid injection and extraction and land use changes have also been associated with surface deformation processes.

Menengai-Subukia in the Central Kenyan rift (**Figure 1**) is a densely populated area with a setting of ground deformation, rifting and human activities like drilling geothermal wells and groundwater abstraction for domestic use. Geothermal activities in Menengai began in 2011 with the drilling of three power plants. The Menengai Geothermal project is located approximately 30 km north of Nakuru city. It started in 2014; and originally, the project targeted 50 wells to generate enough steam to produce more than 50 MW. 49 wells had been drilled by the end of November 2019, to produce a capacity of 169.9 MW; which had exceeded the initial estimated capacity [2]. Geothermal exploration has developed and has been increasing, whereby hydrothermal fluids e.g., steam, have been extracted from the ground. Human population has also increased, leading to demand for more resources like water, leading to increased rate of groundwater extraction like borehole drilling.

Calderas have the potential for extremely large eruptions; therefore, there is a need to distinguish between the semi-continuous unrest seen at many calderas and the precursors to a large eruption. It is important to identify the areas of surface deformation and to understand their relationship with geological structures and environmental factors. Prediction of surface dynamics will help in taking appropriate decisions regarding geothermal exploration and land use activities.

The Menengai caldera, is among the volcanoes located along the densely populated East African Rift, which showed geodetic activity between 1997-2008 [3]. Scarce research has been done in Menengai and its surroundings (Nakuru, Bahati-Subukia) concerning deformation and its probable causative factors using satellite imagery since 2009. Surface deformations are often associated with hazards like foundation collapse and earthquakes, leading to great loss of property and even life. Tectonic movements associated with the East African Rift formation has resulted in deep faults and magmatic intrusions extending to the surface [4]. Several volcanoes have no record of historical volcanism and no real-time monitoring; especially those volcanoes located along the densely populated Kenyan portion of the East African Rift such as Longonot, Menengai and Suswa.

Surface deformation monitoring and structural mapping can be carried out using conventional ground-based techniques such as levelling and Global Navigation Satellite Systems (GNSS) [5]. However, these methods are not efficient and cost effective enough especially when mapping large areas. Recent advances in remote sensing technology has enabled the Interferometric synthetic aperture radar (InSAR) technique to be employed in detecting and monitoring ground deformation successfully in many countries [6]. This study aims to make use of the available sentinel images for continuous monitoring of deformation, in which other techniques were limited due to the discontinuity of data acquisition and limited datasets. This research is not only limited to the caldera; but it also expands on Menengai caldera and its environs; to include the Menengai Geothermal Field, and Nakuru-Subukia area. Full-scale geothermal exploitation and increased human settlement have been projected for this area, which is likely to continue in the future.

## 2. Study Area

Menengai-Subukia area in Nakuru is located at the Kenyan segment of the East African Rift system and hosts the Menengai caldera which is located 36°3'30"E, 0°4'30"S, and 36°20'0"E, 0°15'30"S on the floor of the Kenya Rift Valley; 24 km south of the equator (Figure 1). Menengai Caldera is one of the main topographic features in Nakuru; and one of the major high temperature geothermal fields in Kenya [7]. Menengai caldera hosts both human-induced and natural geothermal activity.

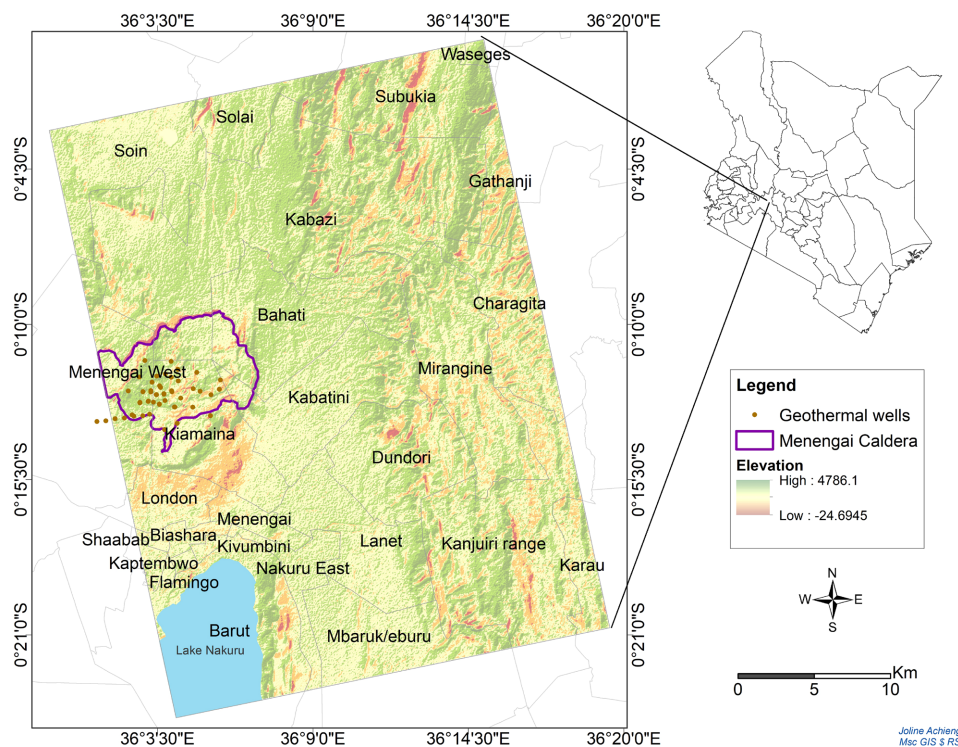


Figure 1. Menengai-Subukia area, in the Kenyan Rift system.

This region is in a geothermally active area, where steam extraction and Kenya's geothermal development projects are located. It is also an area where tectonic and geological surface processes are active. In addition, due to the population growth, land use related water extraction and other activities like agriculture and infrastructural development is increasing. Due to the multitude of land use activities including steam and water abstraction and geological setting, land subsidence and sinking is of primary concern. The geological setting of the area facilitates intense faulting and tectonism. Therefore, ground deformation monitoring has implications to geotechnical aspects and potential risks related to geological hazard.

### 3. Materials and Methods

#### 3.1. Deformation Mapping

Sentinel 1 data was downloaded from the European Space Agency website (<https://scihub.copernicus.eu/dhus/#/home>) and processed in the Sentinel Application Platform (SNAP) software using the Terrain Observation with Progressive Scans SAR (TOPSAR) interferometry technique. These datasets included seven Sentinel 1A images acquired between years 2015-2021 of Menengai area.

The procedure for deformation is as summarized in the diagram (Figure 2) and the steps explained in the subsequent paragraphs.

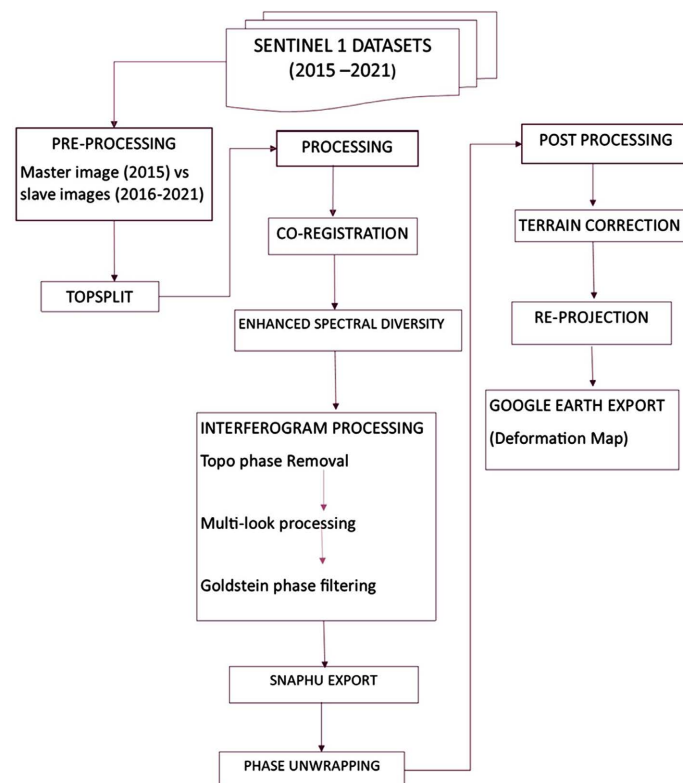


Figure 2. Workflow for generating the interferograms and deformation maps [8].

One Sentinel 1 C-band image in each year was taken from around the same period: in ascending mode. The passes were processed to get a high resolution SAR image of the whole area and to choose an image that would avoid foreshortening around the area of interest.

A pair of images was selected; a primary and a secondary image. The 2015 image was selected as the primary image, whereas 2016, 2017, 2018, 2019, 2020 and 2021 as the secondary images. The burst that just covered the research area was then extracted from the images by splitting them. The process and all the steps to be applied were first defined to enable batch processing of the images [9]. The back geo-coding operator co-registered the two Sentinel 1 split products (primary and secondary) of the same sub swath using the orbits of the two products and a Digital Elevation Model (DEM) which is auto generated from the SNAP server. The DEM has a dual function; to estimate and correct for topography in the final interferogram, it is utilized in conjunction with actual knowledge of the satellite orbits. This process produced a differential interferogram, suitable for monitoring and detecting changes on the ground. The DEM provided the best reduction of baseline decorrelation.

Co-registration was done by applying orbit files to provide accurate satellite position and velocity information. This was to ensure that every ground target contributes to the same pixel (range, azimuth) in both the primary and the secondary image [10]. A coherence image estimation from the stack of the co-registered complex images was included. Adequate overlap of adjacent bursts and sub-swaths allowed for continuous ground coverage. Enhanced spectral diversity (ESD) was applied to correct shifts in range and azimuth direction considering the burst overlap areas. The “no data” sections between burst and average over burst overlaps were eliminated using Sentinel 1 TOPS de-burst. The images were resampled to a standard pixel spacing grid in range and azimuth while maintaining the phase information for all bursts in all sub-swaths [11].

The next step was to remove the topographic induced phase from the deburst interferogram. The interferogram was flattened by removing the topographic phase. The operator replicates an interferogram using a reference DEM and subtracts it from the produced interferogram. Multilook processing was applied to enhance the image interpretability by reducing the speckle appearance (phase noise) since averaging over range and/or azimuth resolution cells produced multiple looks [12]. The conversion from slant range to ground range produced an image with less noise and roughly square pixel spacing. Phase filtering of the interferogram was done to reduce phase noise, *i.e.*, the signal-to-noise ratio needs to be increased for visualization or to aid in the phase unwrapping. Interferometric phase can be corrupted by noise from Temporal or Geometric decorrelation, Volume scattering or processing error. Goldstein phase filtering method was applied; where there was loss of coherence, the interference pattern was lost [13].

The data needed for SNAPHU, a two-dimensional phase unwrapping algorithm, to be applied was exported as the last step in the processing stage [14]. The

phase was unwrapped to relate the interferometric phase to the topographic height, that is the elevation (Figure 3). Fringes were visible as arbitrary color cycles on the interferogram. Interferometric fringes are full 2-cycle representations, where each cycle is equal to half of the sensor’s wavelength. The calculation of relative ground motions (topographic variation) between two locations was performed by counting the fringes and multiplying the result by half of the wavelength of the sensor. Then, the satellite distance ( $\Delta R$ ) divided by the transmitted wavelength ( $\lambda$ ) gives the interferometric phase variation ( $\Delta\phi$ ), (Equation 1).

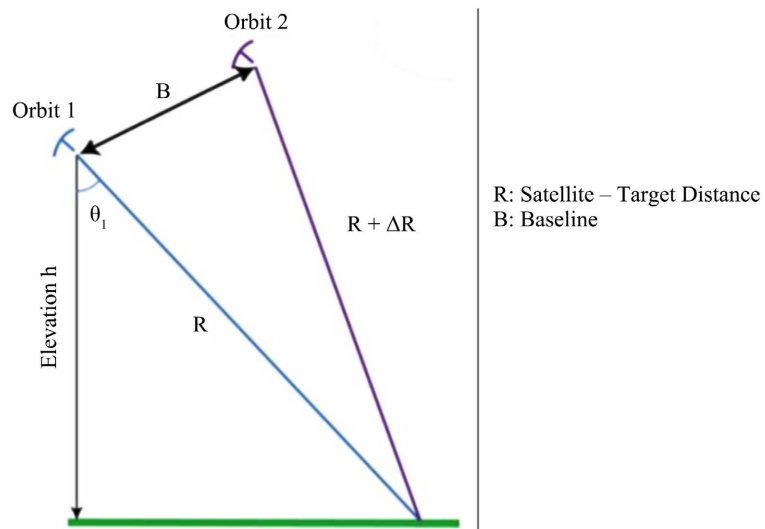


Figure 3. Interferogram formation [8].

$$\phi_1 = \frac{4\pi R}{\lambda}, \quad \phi_2 = \frac{4\pi(R + \Delta R)}{\lambda} \tag{1}$$

$$\Delta\phi = \phi_2 - \phi_1 = \frac{4\pi\Delta R}{\lambda}$$

Interferogram formation:

$\Delta\phi$ : Interferometric variation

$\lambda$ : Transmitted wavelength

Deformation is determined by the spacing of the fringes. The closer the fringes, the greater the rate of deformation on the ground. In a flat terrain, the fringes are parallel and regularly spaced. Similarities in the interferograms were shown by coherence between the primary and secondary images. This was also useful in generating a DEM. Poor coherence is due to errors arising from the orbit (geometric), temporal variations, vegetation, or processing [10].

The unwrapped phase was converted to ground displacement (phase units to length units) along the line of site (LOS). The height values were derived from the unwrapped product to generate deformation maps.

### 3.2. Post Processing

1) Geocoding—distances in the SAR images can be distorted due to topo-

graphical variations of a scene and the tilt of the satellite sensor. To compensate for these distortions, terrain corrections are done. The range doppler terrain correction was applied, to bring the geometric representation of the image as close as possible to the real world [11].

2) Areas with low coherence in the unwrapped phase were masked out; and left with areas with significant coherence. This was done to reduce errors during processing since these errors produced accumulate from the initial pixel to the last.

3) Reprojection and exporting the interferograms—Reprojection was done to ensure all output is displayed in the same spatial reference. The interferograms were exported to google earth for visualization and ArcMap for the final product.

### 3.3. Lineament Mapping

Sentinel 1A radar image (2020) was preprocessed to reduce atmospheric effects that exist in remotely sensed imagery. This was done by orthorectification (speckle filtering and terrain correction) to minimize the existing speckle noise and to geometrically correct it to closely reflect the actual Earth's surface [15]. Speckle noise reduction filtering allows the preservation of the structure in the image data by filtering the homogeneous surfaces and preserving the edges, which is essential in the field of structural geology.

Image enhancement was carried out; whereby four principle directional filters: N-S, E-W, NE-SW, and NW-SE with a  $3 \times 3$  kernel size were applied (Table 1) The angles of the directional filter were assigned as follows: N-S by  $0^\circ$ , NE-SW by  $45^\circ$ , E-W by  $90^\circ$ , and NW-SE by  $135^\circ$ . The kernel size selected in this study was suggested as an optimal kernel size typically used in edge enhancement. This type of filter was used to get a high accuracy in auto extraction of oriented lineaments because the directional nature of Sobel kernels generates an effective and faster way to evaluate lineaments [16].

**Table 1.** Sobel kernels in the four principal directions.

N-S			NE-SW			E-W			NW-SE		
-1	0	1	-2	-1	0	-1	-2	-1	0	1	2
-2	0	2	-1	0	1	0	0	0	-1	0	1
-1	0	1	0	1	2	1	2	1	-2	-1	0

Automatic lineaments extraction in PCI Geomatica was performed based on two main processing steps:

- Detection of edges that gave information on areas of abrupt changes in the values of neighboring pixels, and
- Lines detection.

The following parameters were used during the line module extraction [17] (Table 2).

**Table 2.** Values used for the parameters of the line module.

	Threshold Parameters and Units	Default	Defined
1	RADI (Radius of Filter) (pixels)	10	8
2	GTHR (Edge Gradient Threshold) (range, 0 - 255)	100	60
3	LTHR (Curve Length Threshold) (pixels)	30	20
4	FTHR (Line Fitting Threshold) (pixels)	3	3
5	ATHR (Angular Difference Threshold) (degrees)	30	15
6	DTHR (Linking Distance Threshold) (pixels)	20	20

### 3.4. Land Use Land Cover (LULC) Classification

The data used for classification were Sentinel 2A for 2017, 2019 and 2021 downloaded from ESA Copernicus website. Pre-processing of the cloud free images involved performing atmospheric correction and orthorectification in SNAP. Sentinel 2A has 13 bands in comprising of four bands at 10 m, six bands at 20 m, and three atmospheric correction bands at 60 m spatial resolution [18]. All the image bands were resampled to 20 m resolution.

The images were loaded in ENVI, whereby image subset was done to define the study area extent. Supervised classification was done. The images were displayed in true color composite bands 4, 3, 2 and training sites were developed for six land cover classes. Maximum likelihood algorithm was used, which determines the probability that a given pixel belongs to a certain class by assuming that the data for each class in each band are normally distributed [19]. The results were refined by the smoothing kernel size 3 and aggregation of minimum size 9 and exported to ArcGIS for final output.

## 4. Results

### 4.1. Deformation

The Line of Sight deformation images in this study (**Figure 4**) show that Menengai area is experiencing uplift and subsidence. The rate of subsidence and uplift is recorded in metres ground scale units from Google Earth between the years 2015 and 2021 (**Table 3**).

**Table 3.** Deformation in millimeters of the highest uplift and lowest subsidence for each of the years 2016-2021.

YEAR	Uplift (mm)	Subsidence (mm)
2016	61	104
2017	78	125
2018	103	91
2019	142	62
2020	300	70
2021	350	80

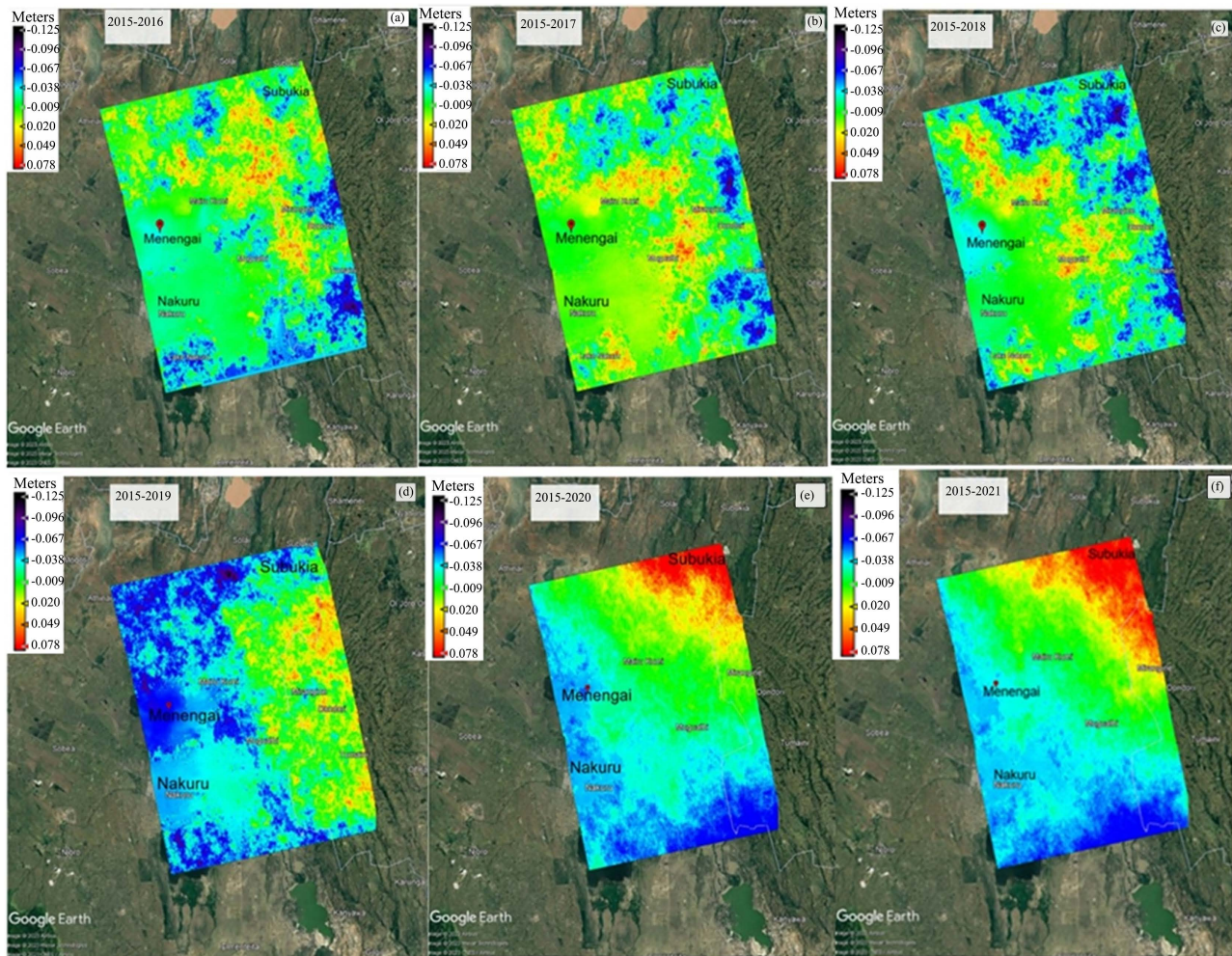


**Figure 4.** (a)-(f): Line of Sight Deformation images in Menengai-Subukia between the years 2015-2016, 2015-2017, 2015-2018, 2015-2019, 2015-2020 and 2015-2021 show subsidence, dark blue color on the extreme whereas positive values indicate an uplift, red color in the extreme.

Areas with low coherence were masked out and left with high coherence (**Figure 5**). Some power plants where drilling projects are happening were selected as reference points within Menengai Geothermal Field. The deformation (scale in meters) changes over the subsequent years, which shows that the ground is under disturbance due to human activities of drilling geothermal wells and hydrothermal fluids discharge. Uplift and subsidence at these points are noted in **Table 4**.

The values of the reference points (power plants) are recorded (**Table 4**). The negative values show subsidence, while the positive values show uplift.

**Table 4.** Deformation of the power plants DFM-004, DFM-001, H and S in metres.

	DFM-004	DFM-001	H	S
Year	173042.1300 E 9981886.854 N	173368.7480 E 9976365.571 N	173571.9152 E 9978414.534 N	175449.6620 E 9973823.392 N
2016	0.002	-0.024	-0.024	-0.024

Continued

2017	0.02	-0.009	-0.009	-0.009
2018	0.048	-0.036	-0.008	-0.008
2019	-0.05	-0.018	-0.018	-0.014
2020	-0.07	-0.07	0.02	0.11
2021	0.13	0.03	0.03	0.03

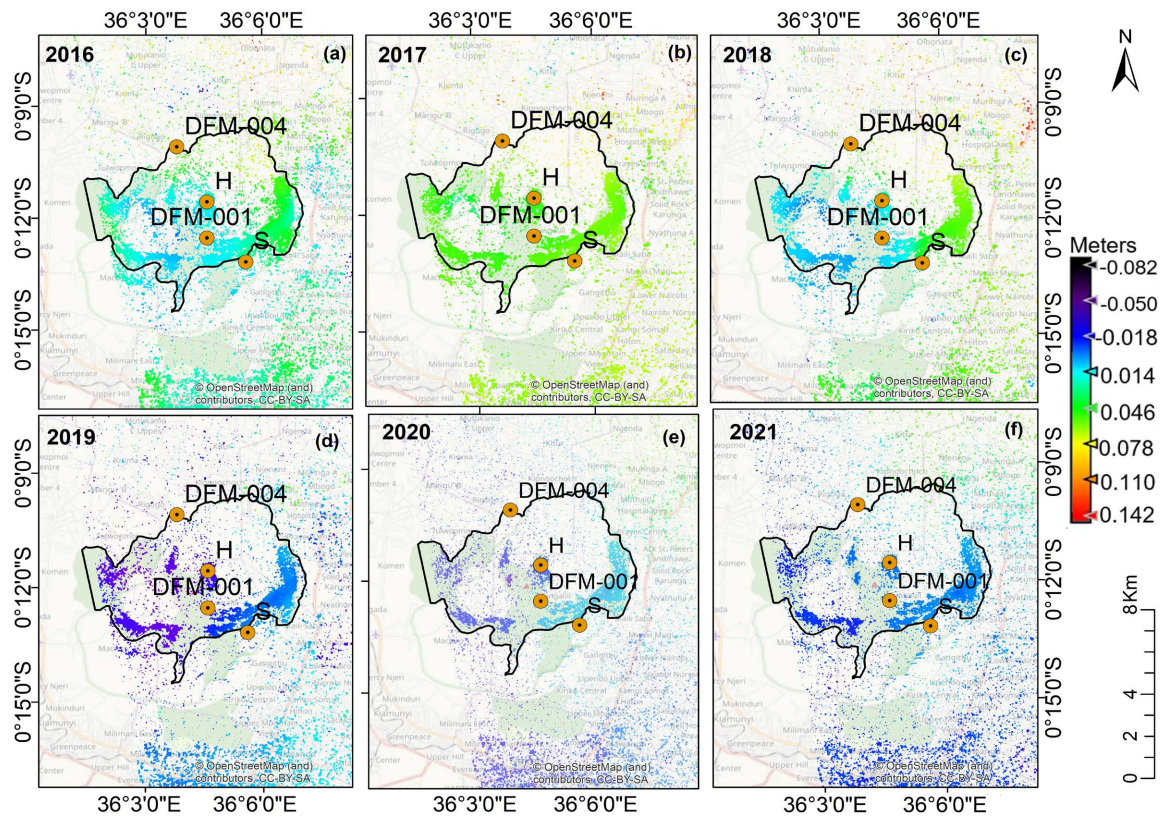


**Figure 5.** (a)-(f): Major deformation areas with reference points (DFM-001, DFM-004, H, S) for the years (2016), (2017), (2018), (2019), (2020) and (2021) within the Geothermal field where geothermal activities are happening.

## 4.2. Lineaments

Lineaments were complimented with rose diagrams to show the orientation and distribution of structures. Lineaments in the NW-SE direction (**Figure 6**) were filtered out to remain with the significant faults that were used to generate the lineament density map.

## 4.3. Lineament Density

Most of the high lineament density values were observed in the north east and south east areas and around Lake Nakuru, while the lower densities of the lineaments were observed southern areas of MGF (**Figure 7**). The high concentration of lineaments in the north east part of the study area could be due to tectonic activity around Menengai Caldera which extends its stress regime to nearby areas; this is manifested by the presence of faults, joints and cracks.

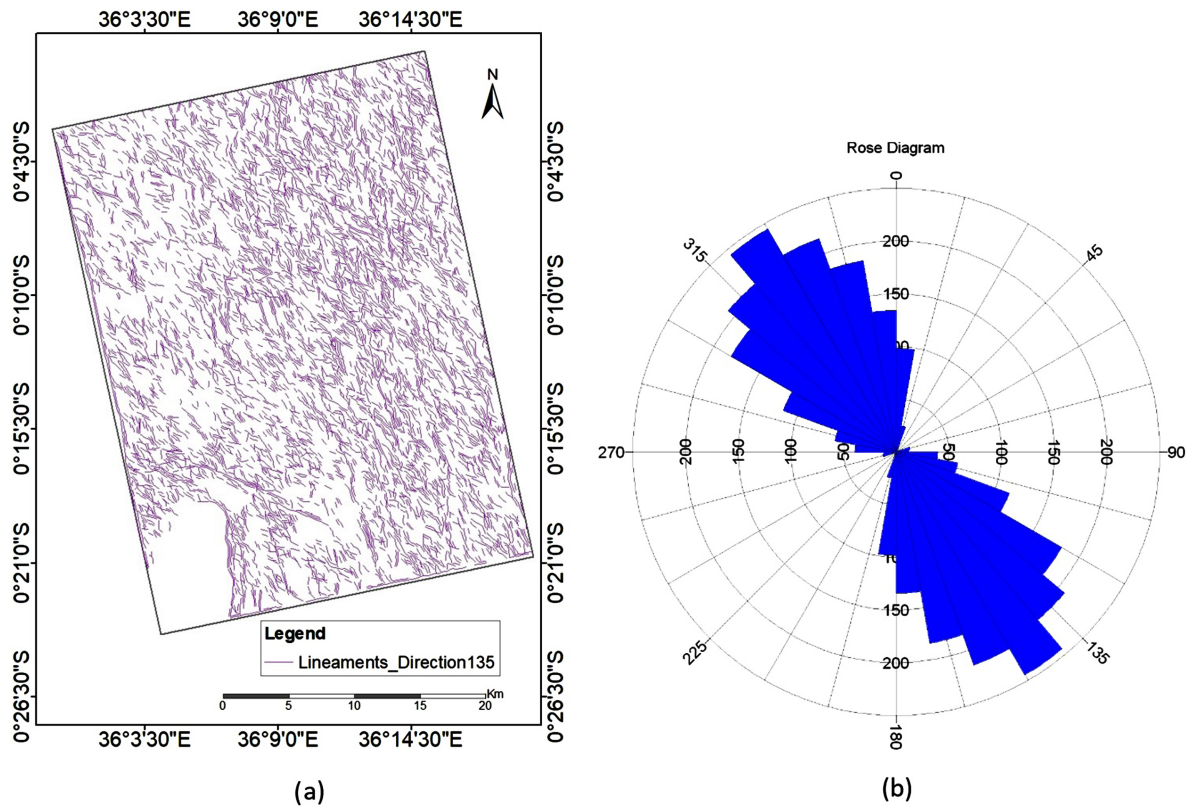


**Figure 6.** (a) Lineaments in NW-SE Direction and (b) Rose diagram showing the orientation and concentration of faults.

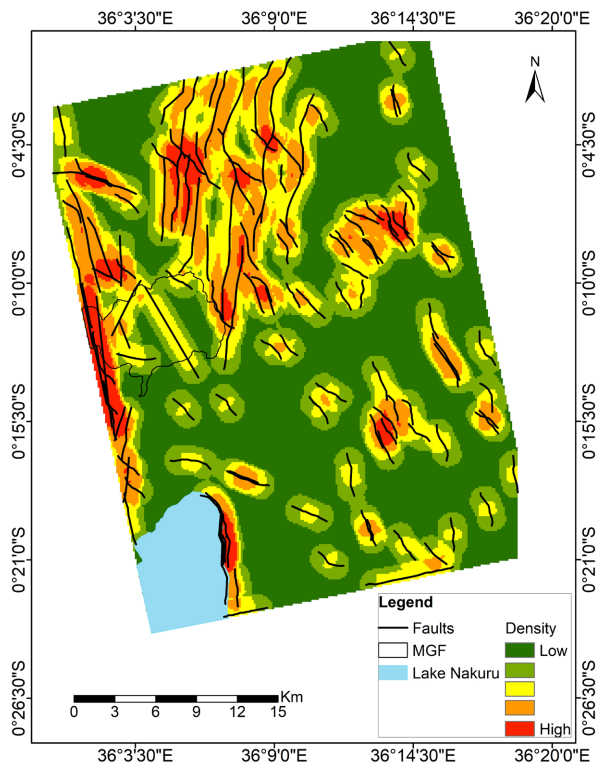


**Figure 7.** Lineament density map. Higher concentration of density values are indicated by a red color, while the lower concentration is in green.

#### 4.4. Correlation Analysis

Correlation analysis was done to assess the relationship between ground deformation and probable causative factors such as active faults and human activities like geothermal, agriculture, building, and construction.

#### 4.5. Deformation and Active Faults

Areas of deformation relative to the active faults in Menengai-Subukia area are shown (Figure 8). The faults in areas around the caldera and in the north eastern side of Menengai have been caused by extension of the stress regime of magmatism leading to deformation in the region.

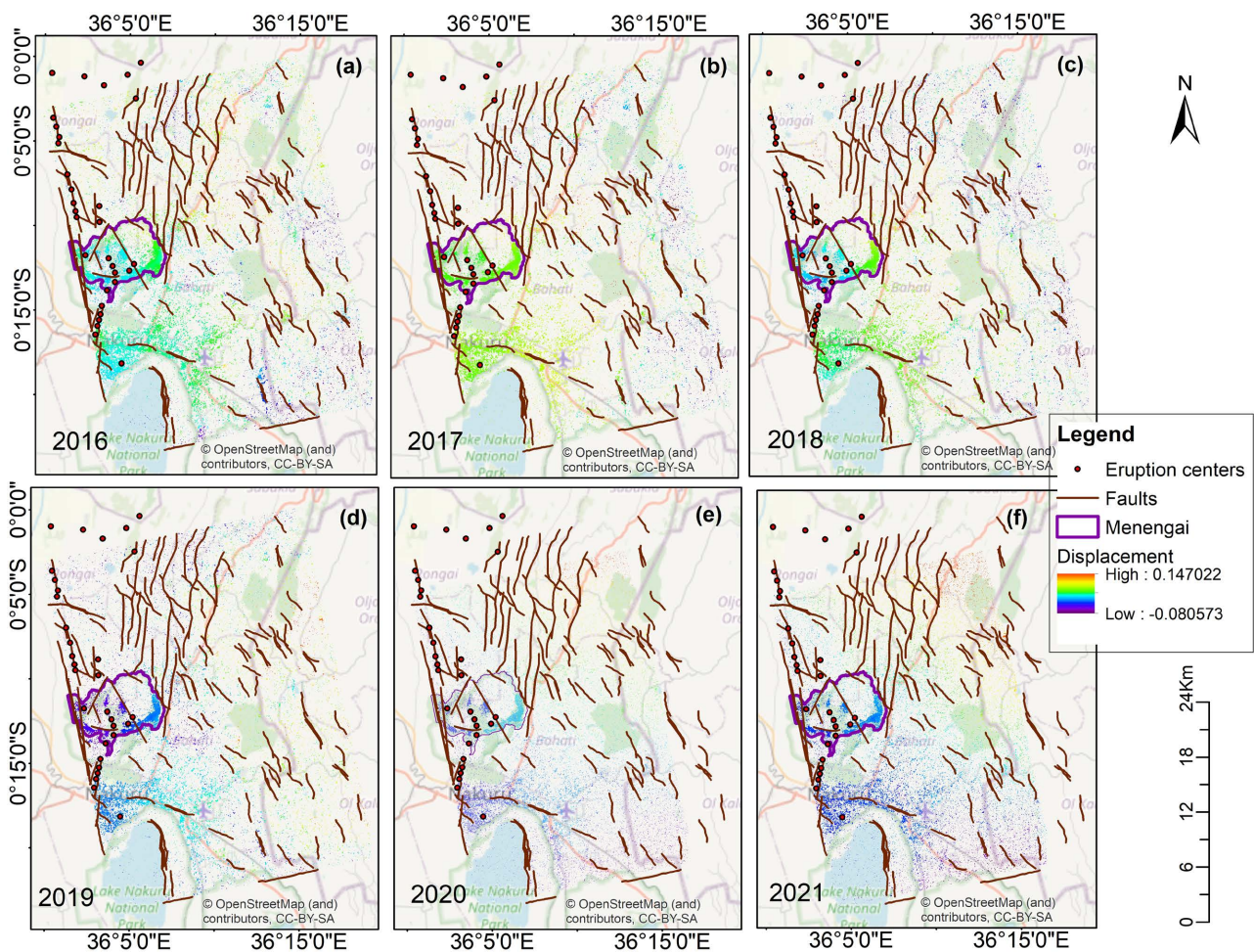


**Figure 8.** Deformation, major faults and eruption centers for 2016-2017. Uplift is shown in red while subsidence is shown in dark blue (low).

The structures, the caldera and the geothermal potential/activity could indicate that magma movement below the ground is still active. Active faults have been found to be in line with the general NW-SE trend of the East African Rift System. These faults are longer and located in areas where the ground has undergone more deformation, especially subsidence (Figure 8). The faults are the

pathways through which hydrothermal fluids came to the surface. The eruption centers that occur mostly along the faults and fissures are indicators of regions where these fluids escape from the ground in form of hot steaming grounds, and hot springs.

#### 4.6. Deformation and Land Use Land Cover

The results in (Figure 9) showed that for the most part, forests and agricultural activities are in the highlands. Most of the built areas are located between MGF and Lake Nakuru. In the year 2017, there were more built areas in the north east regions. Over time, the built areas in those regions reduced and more population is seen closer to Nakuru city and south of MGF in 2021; where infrastructure is more developed. The demand for geothermal energy and water for domestic uses is also increasing around the town. There are more boreholes around the built areas compared to other areas where the land cover is forested, bare land, and grassland. This increase in built areas and thus an increase in population has resulted in greater demand for water, leading to the extraction of greater volumes of fluids.

The Maps (Figure 9) show the land cover and land use accompanied with the land cover percentages (Table 5).

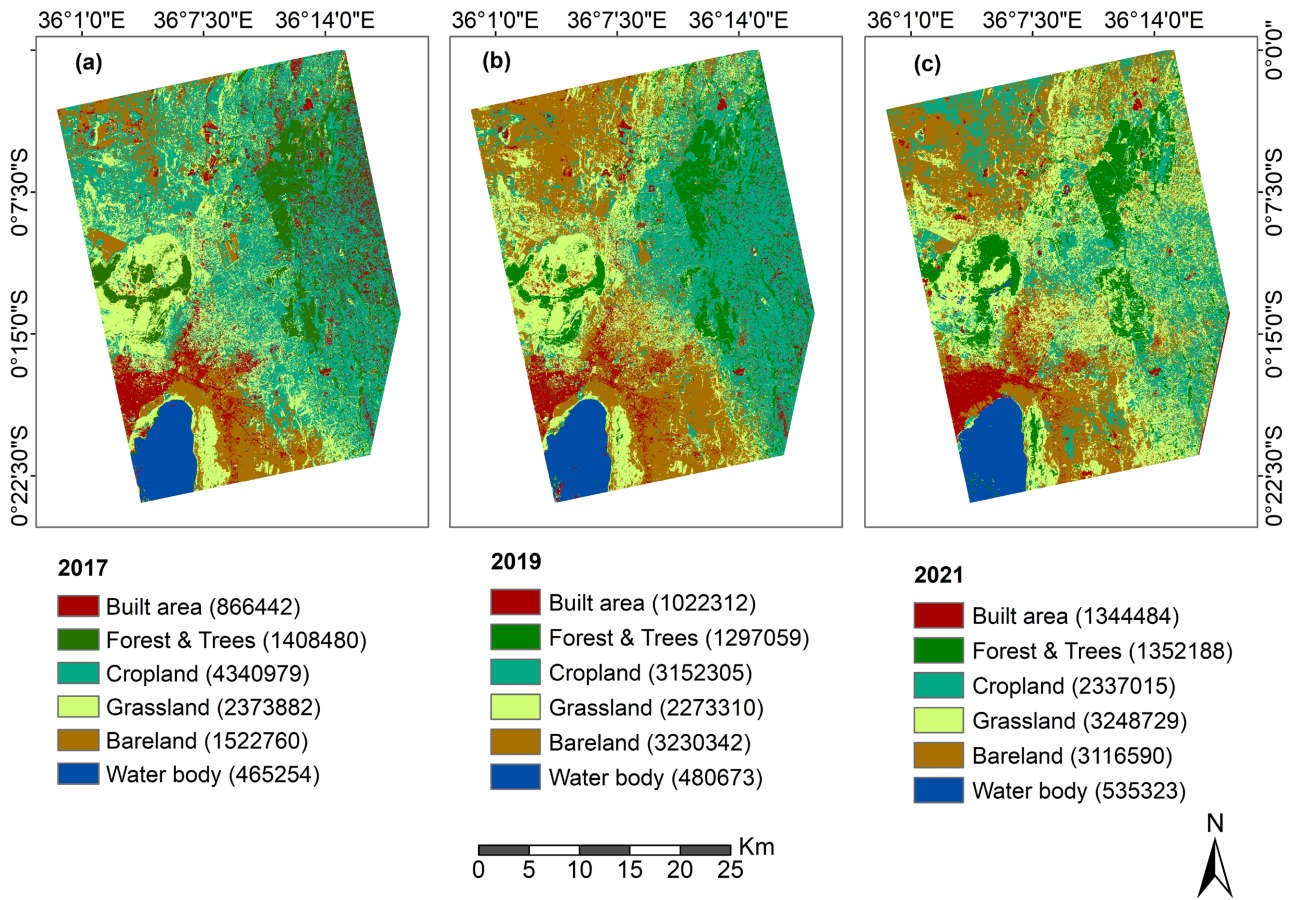
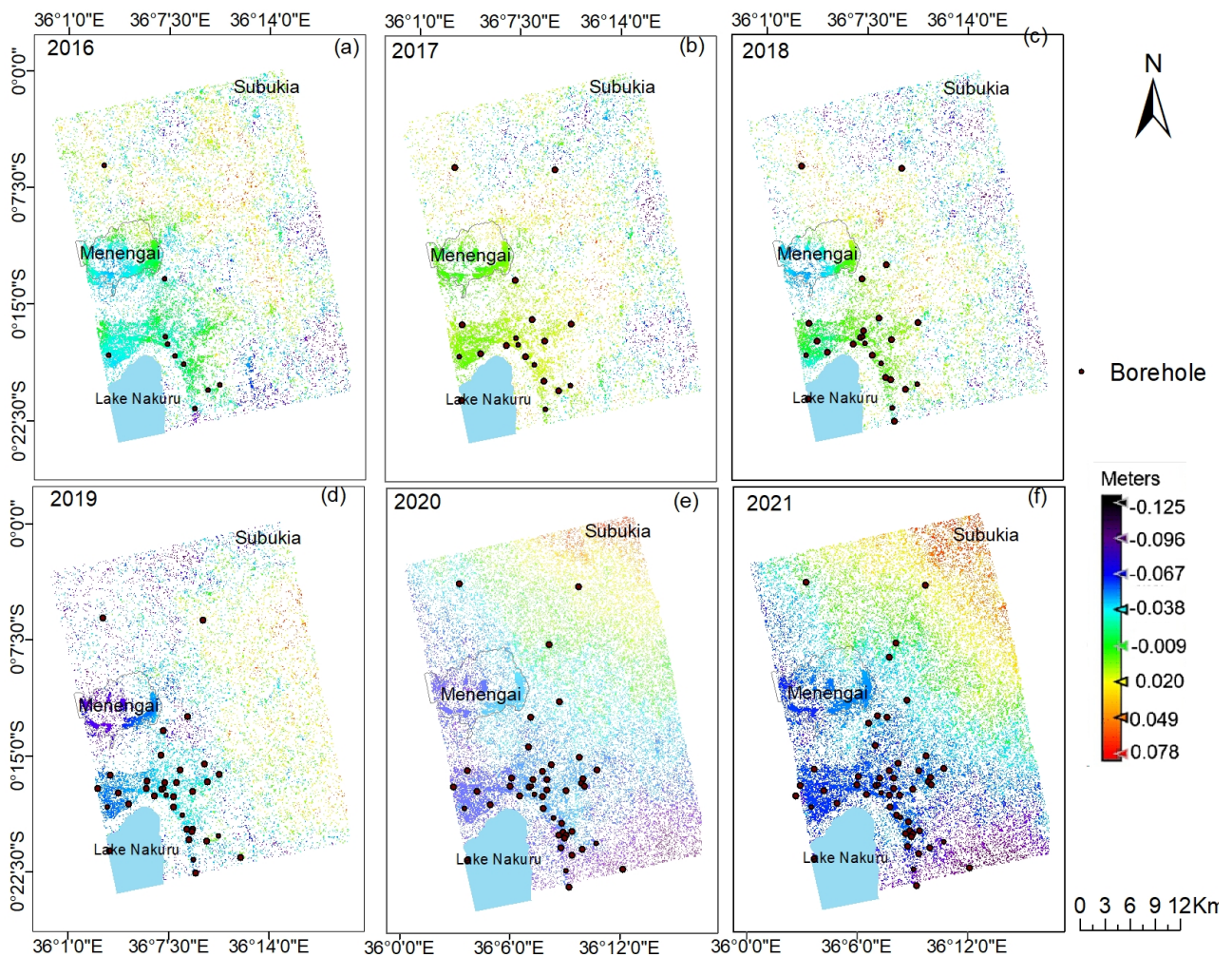


Figure 9. Land cover maps for (2017), (2019) and (2021).

**Table 5.** Land cover classes in percentage.

Land cover Class	2017 (%)	2019 (%)	2021 (%)
Built area	7.89	9.31	12.25
Cropland	39.54	28.72	21.28
Forest	12.82	11.81	12.32
Grassland	21.62	20.71	29.59
Bareland	13.87	29.43	28.39
Water body	4.24	4.37	4.88

Borehole data was obtained from documented records in the Ministry of Water, Sanitation and Irrigation, (MWSI) Kenya. The location of boreholes in Menengai-Subukia and their increase over time between the years 2016-2021 is shown (Figure 10). The number of boreholes in Nakuru county has increased due to the increasing demand for water for domestic use, therefore groundwater abstraction may have contributed to subsidence (Figure 11 and Table 6).



**Figure 10.** (a)-(f): Borehole distribution for the years 2016-2021.

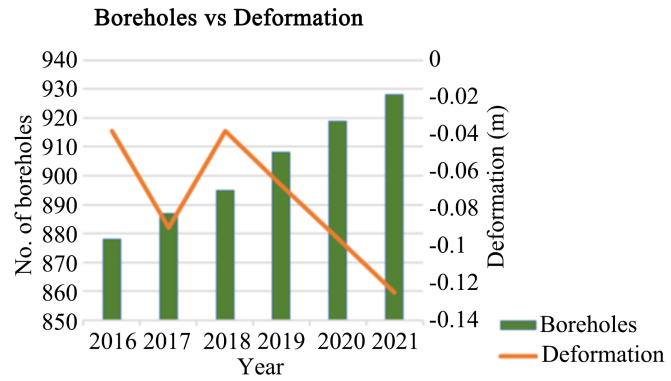


**Figure 11.** Borehole numbers versus deformation rates in Menengai-Subukia area.

**Table 6.** Borehole distribution versus Deformation over time (Borehole data source from MWSI).

Year (by completion dates)	Number of Boreholes	Cumulative Total	Deformation (m)
1900s-2015	872	872	
2016	6	878	-0.038
2017	9	887	-0.09
2018	8	895	-0.038
2019	13	908	-0.067
2020	11	919	-0.096
2021	9	928	-0.125

#### 4.7. Validation

Validation of the deformation maps was done using available GPS data, collected from known points (DFM-004, DFM-001, H, S) for (2015, 2017, 2018 and 2019) (Figure 12).

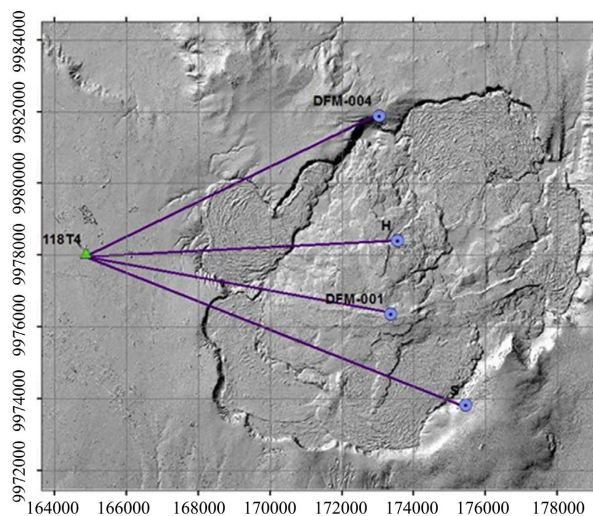


**Figure 12.** Location of Reference points (DFM-004, DFM-001, H, S). Source: (GDC, 2018 internal Report).

The rates of deformation are shown (Tables 7-9) for the years 2017, 2018 and 2019 accompanied with the corresponding deformation graphs (Figures 13-15) respectively. These graphs show comparison in values of the sentinel images (orange color) versus the GPS values (blue color). GPS and elevation data was collected using a differential GPS. This data was compared with the results from deformation maps processed from Sentinel 1 images. The difference in GPS elevation ( $\Delta E$  GPS) was calculated in each year for each of the four reference points (DFM-001, DFM-002, H and S). GPS data from 2015 was used as the reference data, to correspond with the 2015 Sentinel 1 primary image during interferogram processing.

Table 7. Deformation values for 2015-2017.

Reference point	2015 (m)	2017 (m)	GPS $\Delta E$ (m)	Map $\Delta E$ (m)
DFM-004	1962.670	1962.985	0.315	0.02
DFM-001	2154.150	2153.998	-0.152	-0.009
H	1992.735	1992.484	-0.251	-0.009
S	2171.856	2171.964	0.108	-0.009

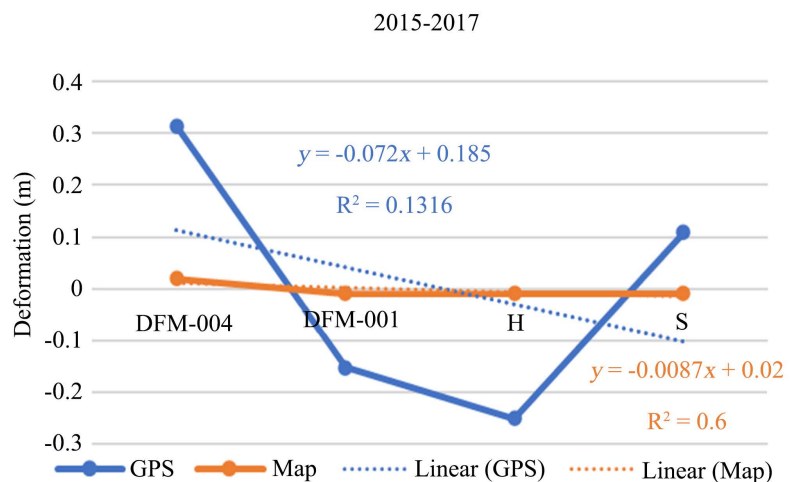


Figure 13. Graph showing deformation from 2015-2017.

Table 8. Deformation values for 2015-2018.

Reference point	2015 (m)	2018 (m)	GPS $\Delta E$ (m)	GPS $\Delta E$ (M)
DFM-004	1962.670	1962.799	0.129	0.048
DFM-001	2154.150	2153.029	-0.121	-0.036
H	1992.735	1992.408	-0.327	-0.008
S	2171.856	2171.854	-0.002	-0.008

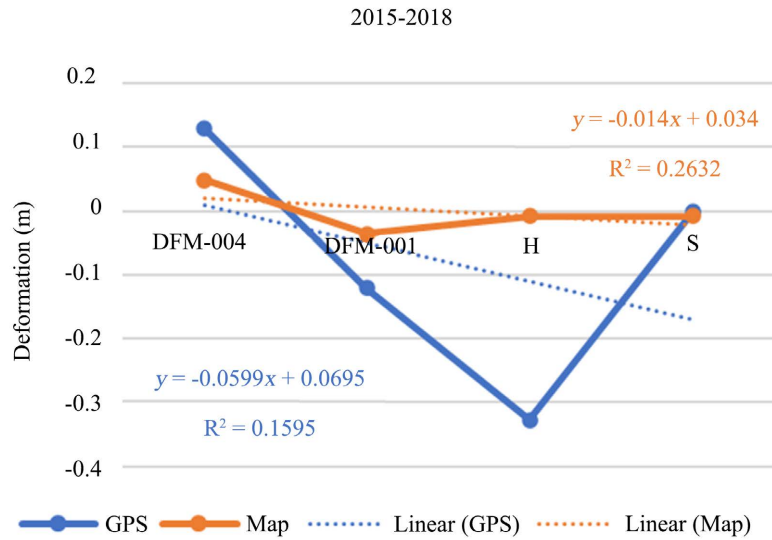


Figure 14. Graph showing deformation from 2015-2018.

Table 9. Deformation values for 2015-2019.

	2015 (m)	2019 (m)	ΔE (GPS)	ΔE (Map)
<b>DFM-004</b>	1962.670	1962.562	-0.108	-0.05
<b>DFM-001</b>	2154.150	2154.038	-0.112	-0.018
<b>H</b>	1992.735	1992.594	-0.141	-0.018
<b>S</b>	2171.856	2172.084	0.228	-0.014

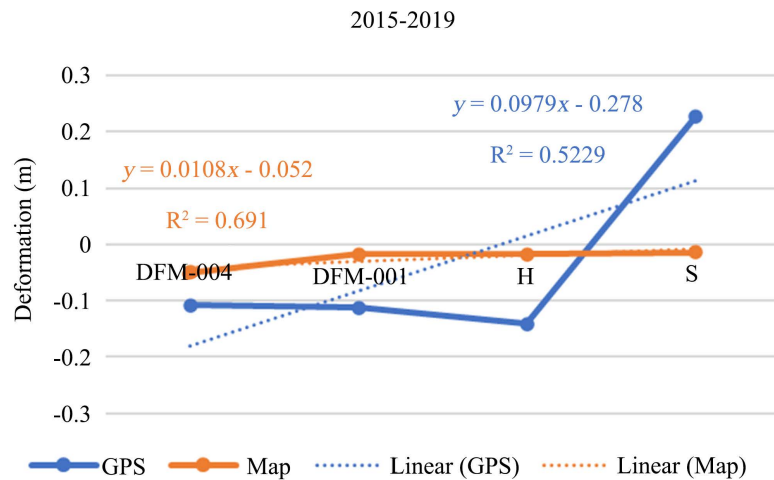


Figure 15. Graph showing deformation from 2015-2019.

The resulting differences in GPS elevation was compared with those from deformation maps. The values were not the same because satellite methods are indicative of the movement (estimation) as compared to terrestrial measurements. This suggests that satellite methods could serve as an indication of the dynamics of ground deformation and be used for reconnaissance surveys.

## 5. Discussion

The processed satellite images (**Figure 4**) have shown progressive deformation over the years. There is significant subsidence in areas around the caldera because of geothermal development whereby geothermal fluids withdrawal rate exceeds the natural rate of replenishment; hence pressure drops in the reservoir, leading to subsidence. Hydrothermal fluids from the ground come to the surface in the form of hot water, steaming grounds, fissures and fumaroles.

The points within the geothermal field (**Figure 16**) are the wells which have been drilled by Menengai geothermal projects. According to GDC internal report [20] recently there exist 63 wells, 27 wells which discharge at a rate of approximately 21 million tons per year. Other wells are in different status; drilling in progress, incomplete, non-productive, reinjection wells, top holed or incomplete, which has led to the area within Menengai geothermal field undergoing significant deformation at different rates.

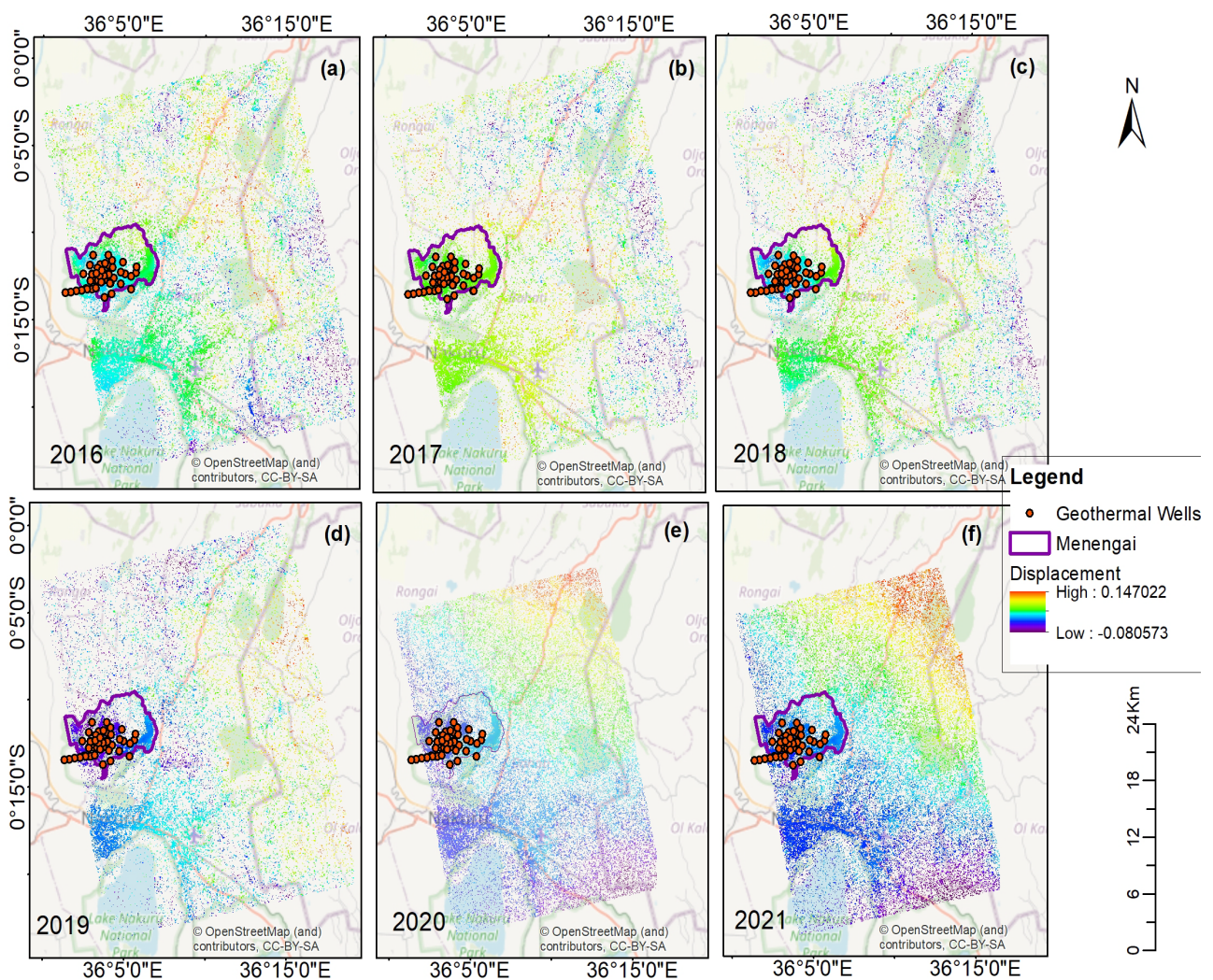


**Figure 16.** (a)-(f): Location of geothermal wells in Menengai. The number of wells has increased from 2016-2021; hence subsequent deformation whereby subsidence is of more occurrence.

The deformation results in this study (**Figure 4**) show that Menengai area is experiencing uplift and subsidence, which are attributed to natural factors like faulting and ascending magma; and human activities such as geothermal drilling projects and ground water abstraction via boreholes. MGF has shown subsidence of 2.4 cm in 2016, 9 cm in 2017, 8 cm in 2018, 5 cm in 2019, 7 cm in 2020 and 3 cm in 2021. A study was undertaken in Kenya rift region to better understand the deformation and tectonics of the East African Rift System [3]. The region exhibits higher temperature geothermal reservoir signatures, including very recent volcanism evidenced by the multiple recent eruptions both inside and beyond the caldera as seen in **Figure 8**. The presence of hot water boreholes, steaming ground, and active fumaroles (with temperatures between 62°C and 88°C) suggests that Menengai sits above an active hydrothermal system [7]. The studies on geothermal resources have led to the drilling of producing wells within the caldera; to verify the presence of such hydrothermal systems. Consequently, three 35 MW power plants are under construction [20].

Geophysical methods can be used to complement or validate the In-SAR technique for measuring ground deformation. It is possible to obtain information on the processes taking place in a volcano that is not erupting using measurements of magnetic fields and gravity. Sub-surface density may be detected by measuring variations in the acceleration due to gravity during magma movement. Magnetometers can also measure changes in the total magnetic field strength induced by magmatic processes.

The relationship between plate motion, intra-rift faults and rift border faults at continental rift settings is usually more complex than at mid oceanic ridges. For example, during extension, pre-existing zones of lithospheric weakness can localize deformation, which, in turn, can cause rift border faults to form oblique to the stretching direction. In some other cases, a pre-existing zone of weakness is orthogonal to the stretching direction [21]. The central Kenyan rift, like the rest of the East African rift, has undergone an extremely complex process of tectonic and geological evolution.

Lineament characteristics that relate to geological displacement have been crucial in tectonic research for the demarcation of identifying structural elements or geological boundaries and exploration of minerals [22]. The analysis of density, trend, and lengths of lineaments is frequently used as the foundation of knowledge for geologists to map structures, deliver pertinent data about energy on a local and regional basis. These structures, located inside the trachyte formation and thought to be the heat source for the geothermal system, may have served as feeder dikes of syenite intrusives [7]. The hydro-thermal system is located at a lithological contact zone where water that interacts with the porous host structure can circulate and is heated by the intrusives within the thick trachyte formation.

Groundwater abstraction has a number of effects on the environment, including changing the hydrologic and hydrogeological regime [23], increasing the danger of groundwater pollution, eradicating groundwater dependent ecosys-

tems, and causing land subsidence [23]. Several methods have been used to identify and quantify land subsidence from excessive groundwater consumption, including conventional levelling surveys, a numerical aquifer modeling, extensometer observations and global positioning systems (GPS) observations. Different levels of land subsidence for various land cover types could be identified by comparing land subsidence and a land cover map, showing that the type of land cover can be a predictor of the volume of groundwater use [23]. The geological formation and availability of water resources have influenced human settlement and agriculture, as can be seen in the land use maps (Figure 9). The built areas are mostly concentrated where there are boreholes, and these are the areas which have also undergone significant subsidence as seen in the deformation maps. Compared to built areas, the other land cover types do not have a strong correlation with deformation. However, with greater environmental data (e.g., rainfall, crop and forest types, and soil erosion), more information can be deduced to assess deformation in areas further away from the MGF.

Although the results acquired from this study were satisfactory, there were some challenges encountered, among them being there is no clear distinction between drilling geothermal wells and drilling boreholes; which of them causes more deformation. The existing borehole data is also not sufficient to correlate deformation and the land cover in other areas besides the built areas. To increase the reliability and decrease uncertainty on this, more ground truthing is required and more aquifer data to enable more analysis.

## 6. Conclusions

This study's main goal was to evaluate ground deformation in Menengai, and correlate with the likely causative factors and its influence in the surrounding regions. The results show that there has been uplift and subsidence between the years 2015-2021 in the Menengai-Subukia area. The MGF has shown subsidence of an average of 2.4 cm in 2016, 9 cm in 2017, 8 cm in 2018, 5 cm in 2019, 7 cm in 2020 and 3 cm in 2021. This is considered large scale because it takes more than decades for such a rate of deformation to occur naturally. This study, however, showed that these deformations occurred in less than a decade.

The automated process of lineament extraction enabled detection of geological structures. After filtering the results of the lineament extraction by comparing fault data on existing structural maps, the active faults were identified. Lineaments were further analyzed using rose diagrams to assess their most frequent directions, which were then compared to the directions of mapped faults. The density map showed that most faults were concentrated at the North East of the Geothermal Field where significant deformation occurs due to tectonic activity.

The land use land cover maps (Figure 9) suggest that human activities consisting of geothermal wells and ground water abstraction were the most influential factors that led to ground deformation in the MGF and in the city, north of Lake Nakuru. Drilling of wells to extract hydrothermal fluids (especially steam),

has resulted in uneven topography. The GPS data used for validation of the reference points within the study area were showed a good part of these data matched the displacement maps.

Continuous monitoring of ground deformation needs to be done in this region to further assess the magnitude of deformation and its major causative factors. To support land use changes, the Revised Universal Soil Loss Equation (RUSLE) analysis could be used to confirm soil erosion has affected deformation in bare land compared to vegetated areas.

Ground truthing and geotechnical logging to assess the rock quality in fault areas can be done to determine the material characteristics of rocks at certain depths. This will assist in assessing the foundation before construction activities in areas prone to geological hazards. Geophysical techniques like gravity, seismic refraction and ground penetrating radar can also be used to determine the depth of hidden faults and fissures. Geochemical analysis of fluid samples could also be used to monitor the behavior of magma below the surface. All these findings could be used to compare and validate data from satellite images.

In the future, to improve these kinds of research studies for deformation, continuous image acquisition and immediate processing should be done to improve the quality of the images and consistency in the final outputs.

## Acknowledgements

Foremost, we thank God for the successful completion of this research.

We acknowledge the following: Joseph Mutua, Dr. Geoffrey Mibei and The Geothermal Development Company (GDC) for the support in the materials needed to achieve the objectives of this research. In addition, the Regional Centre for Mapping of Resources for Development (RCMRD) for availing their facility for research, The Ministry of Water, Sanitation and Irrigation (MWSI) for providing data, Wayne Belcher of the U.S Geological Survey (USGS) for his academic review, and family for their continued support.

## Conflicts of Interest

The authors declare no conflicts of interest regarding the publication of this paper.

## References

- [1] Biggs, J., Ayele, A., Fischer, T.P., Fontijn, K., Hutchison, W., Kazimoto, E., Whaler, K. and Wright, T.J. (2021) Volcanic Activity and Hazard in the East African Rift Zone. *Nature Communications*, **12**, Article No. 6881.  
<https://www.nature.com/articles/s41467-021-27166-y>  
<https://doi.org/10.1038/s41467-021-27166-y>
- [2] Theresa, S. (2020) Geothermal Generation in Kenya Picking up Steam to Power National Grid.  
<https://www.esi-africa.com/industry-sectors/generation/kenyas-geothermal-generation-picking-up-steam/>
- [3] Biggs, J., Anthony, E.Y. and Ebinger, C.J. (2009) Multiple Inflation and Deflation

- Events at Kenyan Volcanoes, East African Rift. *Geology*, **37**, 979-982.  
<https://pubs.geoscienceworld.org/gsa/geology/article-abstract/37/11/979/29889/Multiple-inflation-and-deflation-events-at-Kenyan?redirectedFrom=fulltext>  
<https://doi.org/10.1130/G30133A.1>
- [4] Yang, Z. and Chen, W.P. (2010) Earthquakes along the East African Rift System: A Multiscale, System-Wide Perspective. *Journal of Geophysical Research: Solid Earth*, **115**, B12309. <https://doi.org/10.1029/2009JB006779>
- [5] Uhlemann, S., Smith, A., Chambers, J., Dixon, N., Dijkstra, T., Haslam, E., Meldrum, P., Merritt, A., Gunn, D. and Mackay, J. (2016) Assessment of Ground-Based Monitoring Techniques Applied to Landslide Investigations. *Geomorphology*, **253**, 438-451. <https://doi.org/10.1016/j.geomorph.2015.10.027>
- [6] Hooper, A., Bekaert, D., Spaans, K. and Arikan, M. (2012) Recent Advances in SAR Interferometry Time Series Analysis for Measuring Crustal Deformation. *Tectonophysics*, **514-517**, 1-13. <https://doi.org/10.1016/j.tecto.2011.10.013>
- [7] Kanda, I., Fujimitsu, Y. and Nishijima, J. (2019) Geological Structures Controlling the Placement and Geometry of Heat Sources within the Menengai Geothermal Field, Kenya as Evidenced by Gravity Study. *Geothermics*, **79**, 67-81. <https://doi.org/10.1016/j.geothermics.2018.12.012>
- [8] Veci, L. (2016) Sentinel-1 Toolbox Interferometry Tutorial. <https://forum.step.esa.int/uploads/default/original/2X/6/6648c55d1f642aaf3be7bb4cddd27d0179940830.pdf>
- [9] Braun, A. (2021) Sentinel-1 Toolbox Time-Series Analysis with Sentinel-1. July 2020, 1-31.
- [10] Part B InSAR Processing: A Practical Approach (n.d.).
- [11] Shirzaei, M., Bürgmann, R. and Fielding, E.J. (2017) Applicability of Sentinel-1 Terrain Observation by Progressive Scans Multitemporal Interferometry for Monitoring Slow Ground Motions in the San Francisco Bay Area. *Geophysical Research Letters*, **44**, 2733-2742. <https://doi.org/10.1002/2017GL072663>
- [12] Braun, A. and Veci, L. (2021) Sentinel-1 Toolbox SAR Basics Tutorial. Esa, March, 1-20.
- [13] Goldstein, R.M. and Werner, C.L. (1998) Radar Interferogram Filtering for Geophysical Applications. *Geophysical Research Letters*, **25**, 4035-4038. <https://doi.org/10.1029/1998GL900033>
- [14] Chen, C.W. and Zebker, H.A. (2001) Two-Dimensional Phase Unwrapping with Use of Statistical Models for Cost Functions in Nonlinear Optimization. *JOSA A*, **18**, 338-351. <https://doi.org/10.1364/JOSAA.18.000338>
- [15] Argenti, F., Lapini, A., Alparone, L. and Bianchi, T. (2013) A Tutorial on Speckle Reduction in Synthetic Aperture Radar Images. *IEEE Geoscience and Remote Sensing Magazine*, **1**, 6-35. <https://doi.org/10.1109/MGRS.2013.2277512>
- [16] Kocal, A., Duzgun, H.S. and Karpuz, C. (2004) Discontinuity Mapping with Automatic Lineament Extraction from High Resolution Satellite Imagery. *International Archives of the Photogrammetry, Remote Sensing and Spatial Information Sciences—ISPRS Archives*, **35**, 2.
- [17] Thannoun, R.G. (2013) Automatic Extraction and Geospatial Analysis of Lineaments and Their Tectonic Significance in Some Areas of Northern Iraq Using Remote Sensing Techniques and GIS. *International Journal of Enhanced Research in Science Technology & Engineering*, **2**, 1-11.
- [18] Ge, W., Cheng, Q., Tang, Y., Jing, L. and Gao, C. (2018) Lithological Classification

- Using Sentinel-2A Data in the Shibanjing Ophiolite Complex in Inner Mongolia, China. *Remote Sensing*, **10**, Article No. 638. <https://doi.org/10.3390/rs10040638>
- [19] ENVI Tutorials (2001) <https://13harrisgeospatial-webcontent.s3.amazonaws.com/tutorials/pdfs/ENVIMachineLearningTutorialUnsupervisedClassification.pdf>
- [20] Leader, T., Members, T., Bah, T., Engineer, S.P., Arfaoui, Y., Renewable, C., Specialist, E., Ntoampe, K., Environmentalist, P., Hassane, M., Specialist, P.P., Mciver, D., Counsel, P.L., Kanonda, F., Analyst, S.F., Aron, R., Social, S., Specialist, D., Ngode, E. and Reviewer, E.P. (2011) Project: Country: Menengai Geothermal Development Project Kenya Project Appraisal Report Technical Annexes.
- [21] Agostini, A., Corti, G., Zeoli, A. and Mulugeta, G. (2009) Evolution, Pattern, and Partitioning of Deformation during Oblique Continental Rifting: Inferences from Lithospheric-Scale Centrifuge Models. *Geochemistry, Geophysics, Geosystems*, **10**, Q11015. <https://doi.org/10.1029/2009GC002676>
- [22] Lloyd, R., Biggs, J., Wilks, M., Nowacki, A., Kendall, J.M., Ayele, A., Lewi, E. and Eysteinnsson, H. (2018) Evidence for Cross Rift Structural Controls on Deformation and Seismicity at a Continental Rift Caldera. *Earth and Planetary Science Letters*, **487**, 190-200. <https://doi.org/10.1016/j.epsl.2018.01.037>
- [23] Ahmad, W., Choi, M., Kim, S. and Kim, D. (2019) Detection of Land Subsidence and Its Relationship with Land Cover Types Using ESA Sentinel Satellite Data: A Case Study of Quetta Valley, Pakistan. *International Journal of Remote Sensing*, **40**, 9572-9603. <https://doi.org/10.1080/01431161.2019.1633704>